# Phase transition hysteresis at the antiferroelectric-ferroelectric boundary in $PbZr_{1-x}Ti_xO_3$

Zheyi An,[1,*] Shanshan Xie,[1,*] Petr Ondrejkovic,[2] Pavel Marton,[2] Esther de Prado,[2] Hiroko Yokota,[3] Wei Ren,[1] Zuo-Guang Ye,[4] A. M. Glazer,[5,†] Marek Paściak,[2,‡] and Nan Zhang[1,§]

[1]*Electronic Materials Research Laboratory, Key Laboratory of the Ministry of Education & International Center for Dielectric Research, School of Electronic Science and Engineering, Xi'an Jiaotong University, Xi'an 710049, China*

[2]*FZU-Institute of Physics of the Czech Academy of Sciences, Na Slovance 2, 182 21 Prague 8, Czech Republic*

[3]*Department of Physics, Chiba University, 1-33 Yayoi-cho, Inage-ku, Chiba City 263-8522, Japan and JST PRESTO, 7 Goban-cho, Chiyoda-Ku, Tokyo, 102-0076, Japan*

[4]*Department of Chemistry and 4D LABS, Simon Fraser University, 8888 University Drive, Burnaby, British Columbia, Canada V5A 1S6*

[5]*Department of Physics, University of Oxford, Parks Road, Oxford OX1 3PU, United Kingdom and Department of Physics, University of Warwick, Gibbet Hill Road, Coventry CV4 7AL, United Kingdom*

(Received 23 March 2022; revised 6 October 2022; accepted 14 November 2022; published 7 December 2022)

$PbZr_{1-x}Ti_xO_3$ exhibits an antiferroelectric-ferroelectric phase boundary at the composition $x \sim 0.06$. Around this boundary, several questions need to be answered, such as the stabilizations of different phases with a small amount of compositional difference, the sequence of phase transitions, the coexistence of crystal structures, and potential applications. In this work, we have carried out systematic structural investigations of single crystals and ceramics with several compositions across the phase boundary. The phase diagram for $x \leqslant 0.07$ has been established. A complex phase coexistence is found near the phase boundary, which leads to an unusual transition sequence. It is confirmed that *Pbam* and *R*3*c* structures maintain a subtle balance at the phase boundary, which may be perturbed by a slight change in the concentration or external stimuli. These findings provide unique insights into understanding the antiferroelectric-ferroelectric competition and, hence, into designing alternative materials for energy storage and conversion.

DOI: 10.1103/PhysRevB.106.224103

## I. INTRODUCTION

Compositional phase boundaries in solid-solution systems of perovskites are of particular interest for applications. The free energy can be relatively flat between the minima for structures on both sides, and this structural instability may lead to enhanced physical properties [1]. In the $PbZr_{1-x}Ti_xO_3$ (PZT) solid-solution system, the morphotropic phase boundary (MPB) at $x \sim 0.48$ separating the *P*4*mm* and *R*3*c* phases is one such boundary. Because of the high piezoelectric properties at the MPB, PZT ceramics are to this day the most widely used piezoelectric materials and have received much attention in fundamental studies [2,3]. On the other hand, another boundary at $x \sim 0.06$ separates the antiferroelectric (AFE) and ferroelectric (FE) phases. PZT and other $PbZrO_3$ (PZ)-based solid solutions have become one of the most promising AFE materials for energy storage and conversion [4]. However, the origin of these properties is poorly understood, especially the structural change under external stimuli and, more fundamentally, a description of the crystal-structure change from the AFE *Pbam* phase ($x < 0.06$) to its neighboring FE *R*3*c* phase ($x > 0.06$). In the following, the "FE phase" will always refer to the low-temperature *R*3*c* ferroelectric phase, whereas AFE will always mean the *Pbam* phase.

In the orthorhombic *Pbam* structure, antiparallel cation displacements along $\langle 110 \rangle_{pc}$ (subscript *pc* denotes the pseudocubic coordinate system throughout this paper) form a superstructure [5,6], and the long-range order of oxygen octahedral $a^- a^- c^0$ tilts (Glazer's notation [7]) are considered to be important in the stabilization of the AFE phase [8–10]. The rhombohedral *R*3*c* structure is featured by ordered cation displacements along $\langle 111 \rangle_{pc}$ and $a^- a^- a^-$ tilts [11]. In ceramics near the boundary, a mixture of *Pbam* and *R*3*c* structures has been observed at room temperature (RT), and the phase fractions depend on the thermal history [12,13]. With increasing temperature, before entering the paraelectric (PE) $Pm\bar{3}m$ phase, both the AFE and FE phases transform into an intermediate (IM) state, in which the shape of the unit cell is similar to that of the rhombohedral structure, and complex superstructure reflections appear in diffuse scattering patterns [14–17]. The distinct existence of the IM state provides an opportunity to observe and analyze the interplay of different structural components during the stabilization processes of the AFE and FE phases. However, there is still a lack of direct experimental investigations of the temperature-induced phase transition on both sides of the phase boundary from the IM state. Therefore, the balance and transition mechanisms among the IM, *Pbam*, and *R*3*c* phases are still unclear.

In this work, we have investigated $PbZr_{1-x}Ti_xO_3$ ($0.04 \leqslant x \leqslant 0.07$) single crystals and ceramics to reveal their local

*These authors contribute equally to this work.
†mike.glazer@physics.ox.ac.uk
‡pasciak@fzu.cz
§nzhang1@xjtu.edu.cn

 

and average structures and the process of transformation with temperature. Optical experiments and x-ray and neutron scattering results show that, near the phase boundary, the AFE and FE structures coexist with a continuously changing ratio as a function of $x$. The AFE components tend to appear as smaller domains with increasing $x$ and finally become a local-structural component upon entering the FE side. An unusual transition path $Pbam \xrightarrow{\text{heating}} \text{IM} \xrightarrow{\text{cooling}} R3c \xrightarrow{\text{resting}} Pbam$ has been discovered near the phase boundary, which is explained by the energy estimation from density functional theory based calculation and thermodynamic analysis.

## II. EXPERIMENTAL DETAILS

### A. Crystal growth

Zr-rich PZT single crystals were grown using the flux-growth method, and the detailed growth conditions are described elsewhere [17]. The Ti concentrations in the as-grown crystals were determined to be between 2% and 8%, which will be discussed in detail in the Results section. One of the crystals in this batch was selected for careful study, and it was polished parallel to the $\{001\}_{pc}$ planes with a thickness of 0.045 mm and in-plane dimensions of approximately $0.3 \times 0.3\,\text{mm}^2$.

### B. Optical measurements

The optical measurements were performed using a polarizing light microscope (PLM, BX51, Olympus). The light passed through the crystal sample after being transmitted through a polarizer and was then focused by an objective lens before passing through an analyzer perpendicular to the polarizer. In the high-temperature experiments, the crystals were heated in a Linkam (THMS600E) heating stage.

### C. Diffuse scattering experiment and data processing details

Diffuse scattering experiments were carried out at Beamline X-Ray Diffraction I at the Elettra Sincrotrone Trieste, Italy. The x-ray energy was set to be 12.8 keV (0.9686 Å), just below the $L_3$ absorption edge of Pb 13.035 keV [18]. The x-ray beam size was $50 \times 50\,\mu\text{m}^2$. Even though there are composition segregations in this crystal, each measured region is small enough to be regarded as homogeneous. Scattering data were accumulated by rotating the crystals around the $\omega$ axis with $\Delta\omega = 0.2^\circ$ steps. The exposure time was 5 s per frame. The intensity was collected by a PILATUS 2M pixel area detector (DECTRIS, Switzerland). The distance between the detector and the crystal was 150 mm. The measurements were carried out at a series of temperatures above RT and below 300 °C with an interval of 5 °C − 10 °C. The data were processed with the SNBL TOOLBOX [19], while reciprocal-space planes were reconstructed with the program CRYSALIS and self-developed MATLAB scripts.

### D. Ceramic preparation, x-ray powder diffraction, and high-resolution neutron diffraction

Ceramic samples $PbZr_{0.96}Ti_{0.04}O_3$, $PbZr_{0.95}Ti_{0.05}O_3$, $PbZr_{0.94}Ti_{0.06}O_3$, and $PbZr_{0.93}Ti_{0.07}O_3$ were used in this study, and the preparation conditions are described in Yokota *et al.* [11].

X-ray powder diffraction experiments were also carried out at Beamline X-Ray Diffraction I at the Elettra Sincrotrone Trieste, Italy. The ceramic samples were held in glass capillaries. To avoid the preferred orientation, scattering data of ten frames were collected and integrated with the capillary being rotated $\Delta\omega = 6^\circ$ for each frame. The exposure time was 10 s per frame. The intensity was collected by a PILATUS 2M pixel area detector, and the integration to a one-dimensional (1D) profile was carried out with FIT2D.

Room-temperature and high-temperature neutron time-of-flight experiments were performed at HRPD, ISIS (Rutherford Appleton Laboratory, UK). Data collected from the back-scattering detector bank were selected for structural refinement, with the highest resolution $\Delta d/d \approx 6 \times 10^{-4}$. Data were collected in the 31–125 ms time of flight windows covering the 0.65–2.59 Å $d-$spacing range.

Rietveld refinement was carried out using TOPAS ACADEMIC [20]. The scale factor, background parameters, peak-shape function parameters, and absorption correction coefficient were refined.

### E. Differential scanning calorimetry (DSC)

The DSC measurements were performed on DSC 250 (TA Instruments), with $PbZr_{0.95}Ti_{0.05}O_3$ ceramic powder (∼7 mg) held in a sealed aluminum crucible. The heating and cooling rates were set as $5\,\text{K}\,\text{min}^{-1}$. The heat flow $dQ/dT$ was measured as a function of temperature. After removing the baseline measured with an empty crucible, we obtained the heat-flow data.

## III. EXPERIMENTAL RESULTS

### A. Room-temperature average structures as a function of compositions

Ceramic samples with compositions near the *Pbam*-*R*3*c* boundary ($x = 0.04$–$0.07$) were studied by high-resolution neutron powder diffraction at room temperature. As shown in Figs. 1(a)–1(c), from $x = 0.04$ to 0.07, Bragg reflections and superstructure reflections (quarter and *R*-point reflections) change continuously. The $002_{pc}$ peaks are split at $x \leqslant 0.06$ and change into an almost single peak at $x = 0.07$ [Fig. 1(a)], indicating a change from orthorhombic to rhombohedral symmetry. The intensities of quarter reflections, with $\mathbf{q}_{\text{AFE}} = \{h \pm 1/4\ k \pm 1/4\ l\}_{pc}$, decrease from $x = 0.04$ to $x = 0.07$ [Fig. 1(b)]. Since quarter-reflection intensities are signatures of antiparallel cation displacements in the *Pbam* structure [5], it can be confirmed that the *Pbam* fraction decreases with increasing $x$. *R*-point reflections, $\{h + 1/2\,k + 1/2\,l + 1/2\}_{pc}$, also change from being split at $x \leqslant 0.04$ to being a single peak at $x = 0.07$ [Fig. 1(c)]. Since *R*-point intensities originate from $a^-\,a^-\,c^0$ oxygen tilts in the *Pbam* structure and $a^-\,a^-\,a^-$ tilts in the *R*3*c* structure [7], the change in the shape of the *R*-point reflection is caused by the difference in phase fractions at different values of $x$. From these peaks, it is estimated that $x = 0.04$ and 0.05 mainly consist of the *Pbam* structure, $x = 0.06$ is a mixture of *Pbam* and *R*3*c*, and $x = 0.07$ has mainly the *R*3*c* phase.

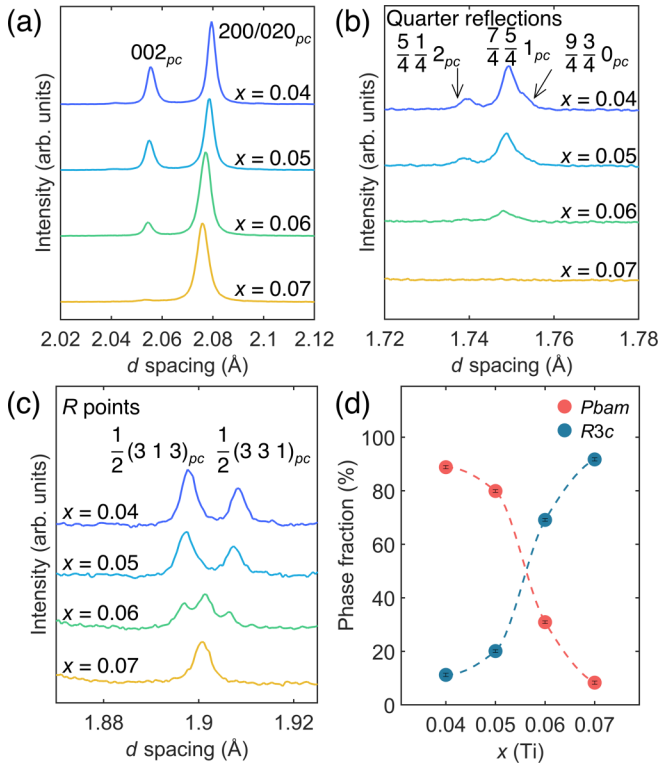


FIG. 1. Neutron powder diffraction results of $PbZr_{1-x}Ti_xO_3$ ceramics ($x = 0.04$, 0.05, 0.06, and 0.07) with (a) change in $\{002\}_{pc}$, (b) quarter reflections, (c) *R* points, and (d) phase fractions obtained from Rietveld refinements. The dashed lines in (d) are guides for the eyes.

The structural transition as a function of $x$ has been further studied by Rietveld refinements [21]. These were carried out with a single *Pbam* phase, a single *R*3*c* phase, and a mixture of *Pbam* + *R*3*c* phases for each composition; the mixed model gives the best fit (Table S1 and Fig. S1 of the Supplemental Material [22]). As shown in Fig. 1(d), in ceramics with $x = 0.04$ and 0.05, the fractions of *Pbam* structure are 88.8(6)% and 79.9(5)%, respectively. With increasing $x$, the *R*3*c* fraction increases monotonously at the expense of decreasing *Pbam* fraction. At $x = 0.06$, the *R*3*c* fraction exceeds its *Pbam* counterpart, which decreases to 30.9(5)%. The sample with $x = 0.07$ mainly consists of the *R*3*c* phase, with only 8.3(6)% AFE phase. Detailed structural models are shown in Table S2 in the Supplemental Material [22].

The average structure and phase transitions in single crystals were studied using PLM. The morphology and domain structures (Fig. 2) show a significant variation among different areas across the crystal, indicating an inhomogeneous Ti-concentration distribution, which is common in lead-based perovskite crystals. The Curie temperatures $T_C$, assigned to each region when it turns into complete optical extinction, show a gradient across the crystal (Table I), ranging from 247 °C at the top continuously to 260 °C at the bottom. Based on the individual behaviors of different regions and transition temperatures into the IM state ($T_{IM}$, shown in Table I), we roughly divide this crystal into three regions, namely, regions A, B, and C [Fig. 2(a)]. By comparing with the phase diagram by Cordero *et al.* [23], the compositions, $x$, are found to be around 0.04 in region A, 0.05 in region B, and 0.06–0.07 in region C [Fig. 2(i)]. Therefore, the composition range of this crystal corresponds to that of the ceramic samples.

The crystal symmetries of the single crystal at RT agree well with the average structures determined by powder diffraction. As shown in Fig. 2(b), the extinction angle for most areas is 45°, consistent with orthorhombic/rhombohedral symmetry. For orthorhombic regions, domains with 0°/90° extinction are rarely observed because most crystals are naturally grown to be plate shaped, and their thickness directions coincide with the crystallographic $c$ axis. Region A is mainly composed of ferroelastic domains larger than 100 $\mu m^2$. Some smaller domains are also observed, as shown in Fig. 2(b) and the region marked by the dashed ellipse in Fig. 2(c), which differ slightly from PZT single crystals with even smaller Ti concentrations [24]. Most small domains are surrounded by regular and straight domain walls, i.e., along $[1\,0\,0]_{pc}$ or $[0\,1\,0]_{pc}$. Upon entering region B, the amount and density of the domain walls become significantly larger. These micrometer-sized domains display irregular shapes, indicating that in the compositions close to the *Pbam*-*R*3*c* boundary, the microstructures on the AFE side are as complex as the crystal structures. On approaching the boundary between regions B and C, the small domains become increasingly more sparse and almost disappear in region C. Based on the structural refinements, especially the fact that the major phase in the $x = 0.04$ and 0.05 samples is orthorhombic *Pbam*, we presume that the small domains are AFE domains, while the large domains in region C are of the FE structure.

### B. Average structure and domain structure changing with temperature

With increasing temperature, all regions transform into the IM state at different temperatures $T_{IM}$. This heating process is shown in Supplemental Movie 1 (see Supplemental Material [22]). A summary of all transition temperatures upon heating and cooling is listed in Table I. At any position of the crystal, the abrupt change of birefringence color reflects the occurrence of phase transitions. If we choose a vertical line across the crystal, the color change and the corresponding temperature vary from the top to the bottom depending on the transition sequence. We plotted this birefringence color change at the black dashed line in Fig. 2(b) at a series of temperatures in Figs. 2(d)–2(f). These could serve as phase diagrams of the crystal since the vertical axis is the composition and the horizontal axis is the temperature. On heating [Fig. 2(d)], the transition happens first in region C (*R*3*c* → IM) at temperatures close to RT, as indicated by the solid line *I* in Fig. 2(d). This phase transition does not cause a change in the domain pattern since the unit cell of the IM state has a pseudorhombohedral shape [17]. Therefore, one may assume that there are not many active domain-wall movements during this phase transition. Ferroelastic domain boundaries along $[1\,0\,0]_{pc}$ and $[0\,1\,0]_{pc}$ can be observed in region C of both phases, which agrees well with our previous quantitative analysis of the domain-wall geometry [24]. The AFE regions B and A transform into the IM state at higher temperatures with an upward moving trend [solid line *II* in Fig. 2(d)], accompanied by intense domain-wall movements.

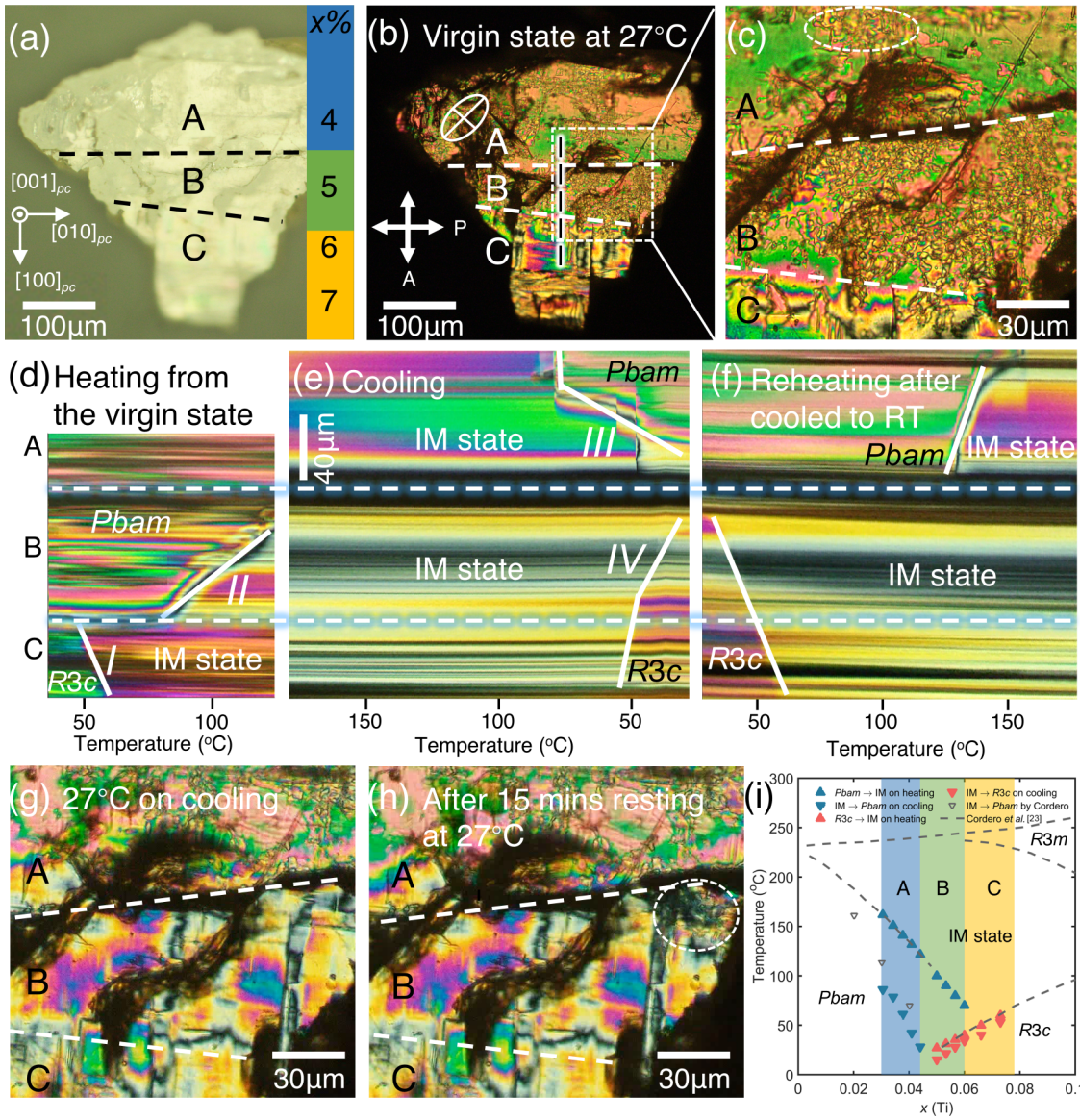


FIG. 2. Optical measurements with the single-crystal sample using PLM. (a) Morphology, positions, and estimated compositions of regions A, B, and C. (b) Domain configurations of the virgin state at 27 °C. (c) Enlarged region of (b) showing microsized domains. The change of birefringence colors of the section marked by the dashed black line in (b) is plotted as a function of temperature upon heating from the virgin state (d), cooling from the cubic phase (e), and reheating after it is cooled to RT (f). (g) The same region as in (c) right after being cooled to RT. (h) After resting for 15 min at RT. The boundaries of regions A, B, and C are marked by the dashed lines in (a)–(h), and the phase transitions in (d)–(f) are marked by the solid white lines. (i) The phase diagram summarizing $T_{IM}$ changing with $x$ obtained by PLM. The dashed lines are reproduced from the phase diagram of Cordero *et al.* [23]. The compositions of several selected regions on the single crystal are estimated by positioning our transition temperatures $T_{IM}$ upon heating on the phase diagram (marked by triangles pointing upward). $T_{IM}$ of the single-crystal sample upon cooling are also marked, by triangles pointing down.

All microdomains are "melted," and the interference colors are significantly changed, corresponding to an abrupt decrease in the overall optical retardation. It is interesting to note that regions A, B, and C behave differently at RT and become homogeneous under the optical microscope in the IM state (Fig. S2 in the Supplemental Material [22]). This indicates that compositions with completely different RT structures are connected by the same IM structure.

Subsequently, this sample was heated through the Curie temperature. A thermal hysteresis of less than 2 °C is observed in region A, and the interference color discontinuously changes to complete extinction on crossing $T_C$ (Fig. S2(b) [22]). These facts indicate the first-order nature of this phase transition. In region B, the Curie temperatures upon heating and cooling have a slight difference (Table I), indicating that it is still a first-order phase transition, consistent with the observations on $PbZr_{0.952}Ti_{0.048}O_3$ single crystal reported by Whatmore *et al.* [25]. The thermal hysteresis in region C is not detectable anymore, which may indicate a second-order transition and confirms the existence of a tricritical point at $x \sim 0.06$, as suggested by Whatmore *et al.* [25].

TABLE I. Average-structure phase transition temperature determined using PLM.

| | $T_{IM}$ on heating | | $T_{IM}$ on cooling | $T_C$ on heating | $T_C$ on cooling |
|---|---|---|---|---|---|
| Region A | 130 °C (bottom) to 163 °C (top) | | 30 °C (bottom) to 86 °C (top) | 247 °C (top) to 249 °C (bottom) | 245 °C (top) to 247 °C (bottom) |
| Region B | Heated from the virgin state: *Pbam* → IM state<br>Heated immediately after cooled to RT: *R*3*c* → IM state | 70 °C (bottom) to 130 °C (top)<br>27 °C (top) to 40 °C (bottom) | Two-step transition:<br>(1) IM → *R*3*c*: 27 °C (top) to 34 °C (bottom)<br>(2) *R*3*c* → *Pbam*: slow regrowth of *Pbam* domains | 248.5 °C (top) to 251.5 °C (bottom) | 247.5 °C (top) to 251 °C (bottom) |
| Region C | 40 °C (top) to 65 °C (bottom) | | 34 °C (top) to 64 °C (bottom) | 251 °C (top) to 260 °C (bottom) | |

The phase transition process of the entire crystal upon cooling is shown in Supplemental Movie 2 [22]. When cooled to around 86 °C, the top area of region A begins to transform back to the *Pbam* phase, as indicated by the solid line III in Fig. 2(e). It is interesting to note that some of the microdomains do not reemerge exactly at the transition temperature, but appear upon further cooling, as shown in another crystal in Fig. S3 [22]. Also, there is a large thermal hysteresis of around 100 °C between the *Pbam* phase and the IM state. This transition process continues until the sample is cooled to RT, where the phase transition frontier reaches the boundary between region A and region B. Curiously, this transition stops here without turning region B into the virgin AFE state as before heating.

In region C, on the other hand, the phase transition from the IM state to *R*3*c* begins at around 65 °C from the bottom area [solid line IV in Fig. 2(e)]. At around 40 °C, the phase transition frontier arrives at the boundary of regions B and C. It continues moving upwards upon further cooling, indicating that the IM → *R*3*c* transition continues in region B. When cooled to RT (27 °C), most of the area in region B has finished the transition. If we reheat the sample immediately after it is cooled to RT, most of region B transforms into the IM state at 27 °C–40 °C ((Fig. 2(f) and Supplemental Movie 3 in the Supplemental Material [22]), which also confirms that this region is in the *R*3*c* structure upon cooling. Therefore, region B passes through totally different transition processes, depending on whether it is heated from a virgin state (*Pbam*) or a cooled state (*R*3*c*). This history-dependent transition can be clearly seen by comparing the positions of the white dashed transition lines in Figs. 2(d)–2(f). Figure 2(i) is the phase diagram summarizing the transition behavior across the crystal upon heating and cooling. It is also worth noting that the AFE microdomains begin to slowly reemerge in some areas with smaller $x$ in region B by letting it rest for around 15 min after cooling (Fig. 2(h) and Supplemental Movie 2 [22]). It takes a much longer time (differs from sample to sample) to completely transform back to its virgin state. On another crystal sample with a similar composition as in region B, a more complete process from the IM state to the reemergence of microdomains has been recorded after cooling to RT, as shown in Supplemental Movie 4 [22].

### C. Change of local-structural components upon heating

X-ray diffuse scattering (DS) experiments were carried out on the same crystal piece. Four small regions, namely, $P_1$, $P_2$, $P_3$, and $P_4$, were selected to measure [Figs. 3(a)–3(d)], and they correspond to four distinct compositions: approximately $x = 0.04$, 0.05, 0.06, and 0.07, respectively. The DS patterns on the $(hk0)_{pc}$ plane at different temperatures are shown in Figs. 3(e)–3(t), and the integrated intensity changes of the characteristic superstructure reflections as a function of temperature are plotted in Fig. 4.

At $P_1$, quarter-reflection intensities are strong and its phase transition behavior upon heating and cooling is in accordance with classic AFE PZT with less Ti [17], as shown in the first row of Figs. 3 and Fig. 4. The *Pbam* ↔ IM transition happens at $T_{IM}$, manifested by the intensity exchanging among the quarter reflections, the $M$ points, $\{h + 1/2\, k + 1/2\, l\}_{pc}$, and the $R$ points. $P_2$ undergoes the same *Pbam* → IM transition as in $P_1$ upon heating with slightly lower $T_{IM}$. It is worth noting that at $P_1$ and $P_2$ around $T_{IM}$, the intensity weakening at the $R$ points follows a similar trend as for quarter reflections, and the strengthening of $M$-point intensities happens almost simultaneously [Figs. 4(a) and 4(b)]. This indicates that, at $P_1$ and $P_2$, which are mainly formed by the AFE structure, the intensities at the $R$ points come purely from $a^- a^- c^0$ oxygen octahedral tilts.

$P_3$ ($x \sim 0.06$) has a completely different behavior compared with $P_1$ and $P_2$. At this position, *both* the *Pbam* → IM and *R*3*c* → IM transitions are observed. At RT, the intensity of the quarter reflection [Fig. 4(c)] is around 30% of that at $P_1$ and $P_2$, indicating that the *Pbam*/*R*3*c* ratio is close to 3:7 at $P_3$, which agrees with the refined phase fractions in the ceramics [Fig. 1(d)]. When the sample is heated from RT, $M$-point intensity starts to rise immediately; on the other hand, the abrupt decrease of quarter-reflection intensity does not happen until above 60 °C [(Fig. 4(c)]. Therefore, the first appearance of $M$-point intensity must originate from the *R*3*c* → IM transition, which is consistent with the PLM observation of a lower *R*3*c*-IM transition temperature [Fig. 2(i)]. After that, the *Pbam* → IM transition happens, marked by the disappearance of quarter reflections. This also explains that the steep

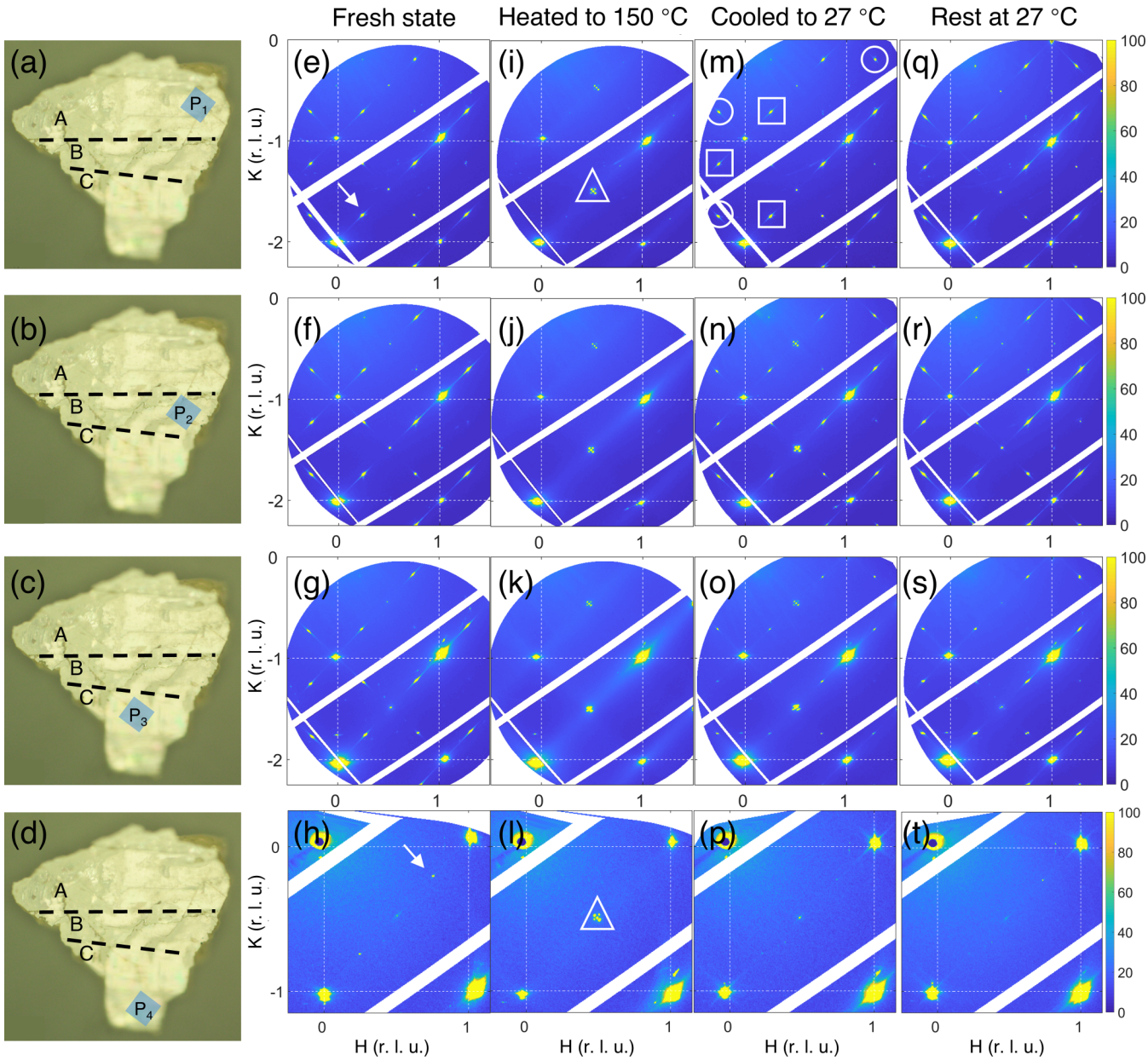


FIG. 3. X-ray diffuse scattering experiment results on the same crystal piece used for PLM studies. (a)–(d) The measured positions, P1–P4, and (e)–(t) DS intensities on the $(hk0)_{pc}$ plane during the phase transition of the single crystal. (e)–(h) Data collected from the virgin-state single crystal at (e) 61 °C and (f)–(h) RT. (i)–(l) Data collected from the crystal heated into the stable IM state at 150 °C. (m)–(p) Data collected from the crystal right after being cooled to RT. (q)–(t) Data collected from the crystal after resting for 7 h at RT. The arrows in (e,h) point to typical quarter reflections, and the triangles in (i,l) indicate a typical $M$ point. From quarter reflections $\mathbf{q}_{\mathrm{AFE}} = (h \pm 1/4 \;\; k \pm 1/4\, 0)_{pc}$, one can identify two ferroelastic domain states, which can be denoted as $\mathbf{q}_{1\mathrm{AFE}} = (h + 1/4 \;\; k + 1/4 \;\; 0)_{pc}$ or $(h{-}1/4 \;\; k{-}1/4 \;\; 0)_{pc}$, and $\mathbf{q}_{2\mathrm{AFE}} = (h{-}1/4 \;\; k + 1/4 \;\; 0)_{pc}$ or $(h + 1/4 \;\; k{-}1/4 \;\; 0)_{pc}$, as a result of the coexistence of $[1\,{-}1\,0]_{pc}$ and $[1\;1\;0]_{pc}$ AFE domains [6]. The squares and circles in (m) indicate the selected quarter reflections $\mathbf{q}_{1\mathrm{AFE}}$ $(1/4\;{-}3/4\;0_{pc},\;\; 1/4\;{-}7/4\;0_{pc},\;\; {-}1/4\;{-}5/4\;0_{pc})$ and $\mathbf{q}_{2\mathrm{AFE}}$ $({-}1/4\;{-}3/4\;0_{pc},\;\; {-}1/4\;{-}7/4\;0_{pc},\;\; 5/4\;{-}1/4\;0_{pc})$, respectively.

decrease in $R$-point intensity does not happen simultaneously with the weakening of the quarter reflections, but right above RT, as part of the $R3c$ $(a^-\,a^-\,a^-) \rightarrow$ IM transition. Details of the $R$-point change are better demonstrated in neutron powder diffraction data. As shown in Fig. 5, $R$-point intensities coming from $a^-\,a^-\,a^-$ in the $R3c$ phase and $a^-\,a^-\,c^0$ in the $Pbam$ phase are both observed at RT. Upon heating to 60 °C, after the $R3c \rightarrow$ IM transition, the intensity at the $R$ point corresponding to $a^-\,a^-\,a^-$ tilts disappears, while the remaining parts from $a^-\,a^-\,c^0$ survive until higher temperatures. In this two-step transition process, only the first step is observed in region C under PLM. This indicates that the $Pbam$ structure appears as local-structural components, which are not observable by optical methods. One may picture the model as AFE components forming small islands in the FE $R3c$ matrix.

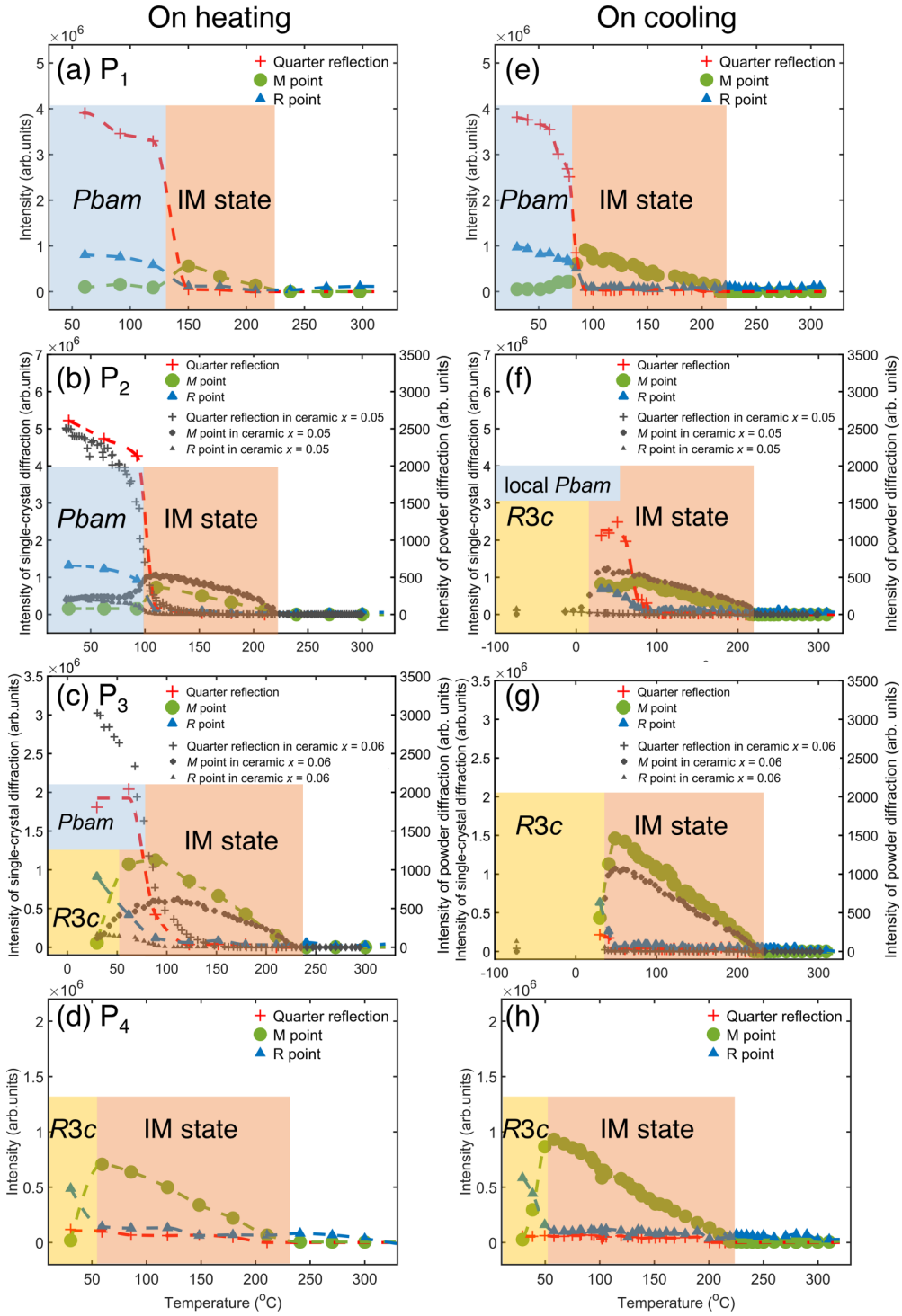


FIG. 4. Integrated DS intensities of superstructure reflections as a function of temperature at all measured positions, namely $P_1$, $P_2$, $P_3$, and $P_4$, during heating (a)–(d) and cooling (e)–(h). DS intensities at quarter reflections, $M$ point $(1/2\ -1/2\ 0)_{pc}$, and $R$ point $1/2(-3\ 1\ -1)_{pc}$ were integrated. Quarter-reflection intensity was averaged over six selected reflections, namely, $1/4\ -3/4\ 0_{pc}$, $1/4\ -7/4\ 0_{pc}$, $-1/4\ -5/4\ 0_{pc}$ ($\mathbf{q}_{1AFE}$), and $-1/4\ -3/4\ 0_{pc}$, $-1/4\ -7/4\ 0_{pc}$, $5/4\ -1/4\ 0_{pc}$($\mathbf{q}_{2AFE}$). The dashed lines are guides for the eyes. For comparison, the integrated quarter reflection $3/4\ 3/4\ 0_{pc}$ (gray cross), $M$ point $3/2\ 1/2\ 0_{pc}$ (gray dot), and $R$ point $1/2(3\ 1\ 3)_{pc}$ (gray triangle) intensities were calculated from x-ray powder-diffraction patterns (see Fig. 6 for full patterns on heating and cooling) of ceramics $x = 0.05$ (b),(f) and $x = 0.06$ (c),(g).

When it comes to $P_4$ ($x \sim 0.07$), the very weak quarter reflections [Fig. 3(h)] indicate the negligible AFE proportion and a stabilized FE $R3c$ structure, with the intensities at the $R$ points mainly coming from $a^-a^-a^-$ tilts. The $R3c \rightarrow$ IM transition happens upon slight heating above RT [Fig. 4(d)]. The transition process on cooling [Fig. 4(h)] is a pure inverse of that on heating. When cooled to RT, intensities at the $R$ points are completely recovered (Fig. 4(h) and Fig. S4(l) in the

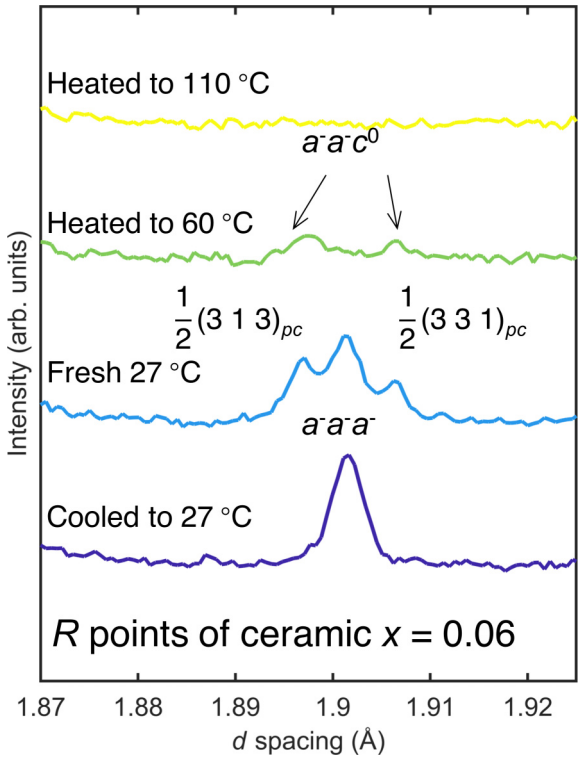


FIG. 5. Neutron diffraction intensities at $R$ points at different temperatures for ceramic ($x = 0.06$). The sample was heated from the virgin state at RT to 230 °C before being cooled to RT.

Supplemental Material [22]), and $M$-point intensities almost disappear completely [Fig. 3(p)].

When heated up to the IM state for all four measured positions, the $M$-point intensities strengthen with the appearance of satellite superstructure reflections [Fig. 3(i)–3(l)]. These features have been well observed in PZT with a smaller amount of Ti [17,26]. However, the incommensurate spots near the $\{h \pm 1/6\, k \pm 1/6\, l\}_{pc}$ position [17] were not observed in this composition range. Similar to the average structures observed by PLM, the IM state displays the same local-structural features across the entire composition range, even though the samples show different structures at room temperature.

### D. Change of local-structural components upon cooling

The sample was cooled from 300 °C subsequently after heating. The measured positions go through a sequence of cubic, IM, and room-temperature phases in general. Details of the complicated IM → RT phase transition are discussed for each distinct composition.

An unusual IM → $R3c$ → $Pbam$ transition was observed at $P_2$ upon cooling. At $P_2$, when cooled to RT, $M$-point intensities were still quite strong, and quarter reflections only recovered to ∼40% of their initial values [Figs. 3(n) and 4(f)]. A ceramic powder sample with a composition similar to $P_2$ ($x = 0.05$) was also measured by synchrotron x-ray diffraction [Fig. 6(a)–6(c)]. When the ceramic sample was cooled to RT, negligible quarter-reflection intensity showed up in the powder-diffraction pattern [Figs. 4(f) and 6(b)]. We subsequently cooled it to even lower temperatures. The $M$-point intensity decreased significantly at around 15 °C,

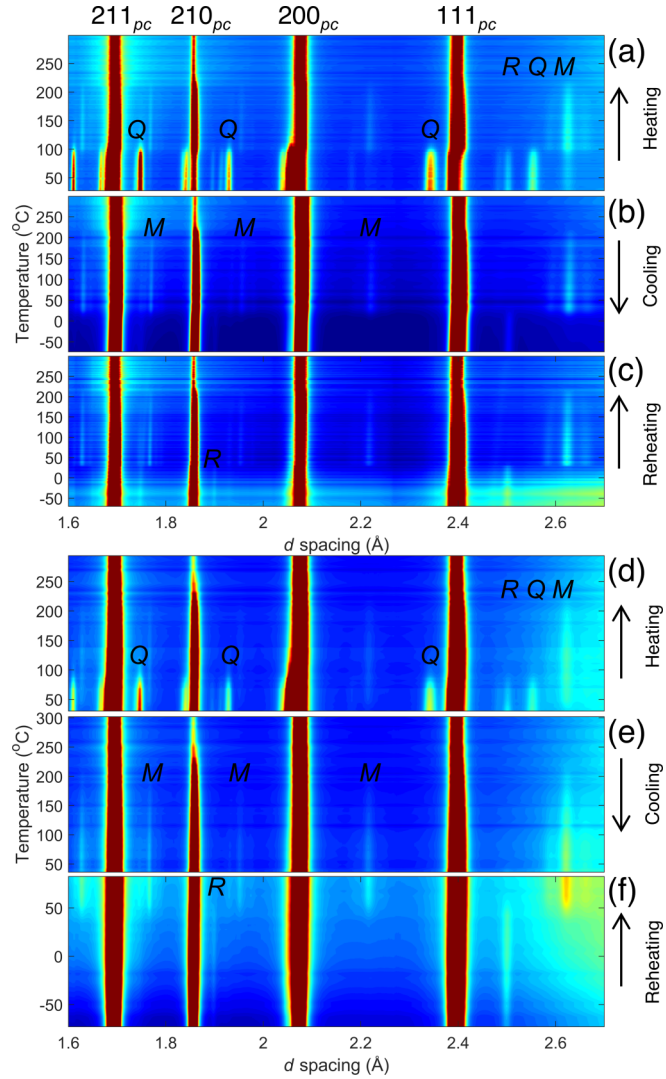


FIG. 6. Variation with temperature of Bragg and superstructure reflections [quarter reflections ($Q$), $M$ points ($M$), and $R$ points ($R$)] of ceramic powders with (a)–(c) $x = 0.05$ and (d)–(f) $x = 0.06$. For both compositions, the sample was heated from the virgin state at RT to 300 °C (a),(d), then cooled to −73 °C (b),(e) before a subsequent reheating process (c),(f).

while the quarter-reflection intensity still did not come back to the value in its virgin AFE state, even when cooled to −73 °C [Fig. 6(b)]. In the meantime, the $R$-point intensity was strengthened to be comparable to its virgin state. These indicate that the IM state transforms to the $R3c$ structure on cooling instead of to $Pbam$ [Fig. 4(f)]. This IM → $R3c$ transition is consistent with the observation in region B under PLM. In addition, similar to the return of microdomains under PLM, in the single-crystal DS experiment reperformed at $P_2$ after resting for 7 h at RT, the intensities of the quarter reflections are found to be strengthened [Fig. 3(r)]. Therefore, it is confirmed that the microdomains in region B are indeed of AFE nature. For this composition, we can conclude that upon cooling from the IM state, the $R3c$ structure becomes dominant first, although it is metastable. On the contrary, the AFE state is more stable, but the formation of a long-range phase takes a longer time.

TABLE II. The energies in meV/f.u. (formula units) of structures optimized with *ab initio* calculations for different $x$ (number of Ti atoms per 64 $B-$site positions in the $4 \times 4 \times 4$ pseudocubic supercell). Energies of the $Pc-$derived structures are estimated as explained in Fig. S5 of the Supplemental Material [22].

| Structure \ $x$ | 0/64 (0) | 1/64 (0.016) | 2/64 (0.031) | 3/64 (0.047) | 4/64 (0.063) | 5/64 (0.078) |
|---|---|---|---|---|---|---|
| *Pbam* | 0 | 0 | 0 | 0 | 0.5 | 1.2 |
| *R*3*c* | 2.8 | 1.9 | 1.0 | 0.8 | 0 | 0 |
| *Pc* (IM) | 61[a] | 58.9 | 56.3 | 53.5 | 51.2 | – |

[a]Reference [17].

Similarly, $P_3$ also undergoes the IM $\rightarrow$ *R*3*c* and the slow *R*3*c* $\rightarrow$ *Pbam* transitions upon cooling, while for this composition, the AFE phase becomes more difficult to re-form. As shown in Fig. 3(s), after resting for 7 h at RT, the quarter reflections are still only partially recovered in DS. The ceramic at $x = 0.06$ undergoes the IM $\rightarrow$ *R*3*c* transition process [Figs. 6(d) and 6(e)], and there is a single peak at the *R* point (Fig. 5) in the diffraction pattern when cooled to RT. This transition process is relatively simple in powder diffraction and PLM, while the slow appearance of the AFE phase–because of its short correlation length–is hard to observe in the average structure.

## IV. THEORETICAL CALCULATIONS AND THERMODYNAMICS OF THE PHASE TRANSITION

To gain further insight into the mechanism of the experimentally observed phase transitions, we have performed structural optimizations for three noncubic phases of Zr-rich $PbZr_{1-x}Ti_xO_3$ using density functional theory based calculations. These were done with the program SIESTA [27] using the same setting as in Ref. [17]. We took into account $4 \times 4 \times 4$ pseudocubic supercells with different Ti concentrations in the solid solution ($N = 0$, 1, 2, 3, 4, and 5). *B* cations were quasirandomly (avoiding nearest-neighbor and next-nearest-neighbor positions) selected from 64 sites to be substituted with $Ti^{4+}$. The resulting compositions are around 0, 0.016, 0.031, 0.047, 0.063, and 0.078. We started with the atomic positions of *Pbam*, *R*3*c*, and *Pc* structures, but already the Zr to Ti substitution breaks the symmetry and in the following conjugate-gradient optimization atoms were not bound to the Wyckoff positions of the original space groups. The overall distortion patterns of the three phases are nonetheless preserved and we keep the space-group labels in the following description.

The energy differences between the studied compositions agree very well with the experimental observations. As shown in Table II, the energies of *Pbam* and *R*3*c* structures are quite close, with a difference of 2.8 meV/f.u. (formula unit) for PZ, and become even closer with increasing $x$. The *Pbam* structure is the most stable one for $x \leqslant 0.047$. At $x \sim 0.05-0.06$, *Pbam* and *R*3*c* structures have close energies, which suggests possible phase coexistence and competition. At $x > 0.06$, the *R*3*c* structure becomes the most stable, consistent with the fact that this structure becomes the major phase. From the evolution of energy as a function of $x$, it can be seen that with more and more Ti doping, the AFE structure is gradually and continuously destabilized, while the *R*3*c* structure is more and more favorable. Unlike for rhombohedral to tetragonal MPB [28], the overall degree of octahedral tilt does not change much with Ti content. However, the Ti-based octahedra are smaller (2.01 Å for Ti-O bond vs 2.11 Å for Zr-O bond) and rotate with a slightly smaller angle. For *Pbam* structures the presence of Ti atoms also adds a small $z$-axis component to off-center displacements of Pb ions.

The estimated energies for the *Pc*-derived structures, which are the main components of the IM state [17], are high for all compositions, and so the IM state should be stabilized in a different way from the *Pbam* and *R*3*c* structures. We performed DSC measurements with $PbZr_{0.95}Ti_{0.05}O_3$ ceramic powder (Fig. 7), to understand these phase transitions from a thermodynamic point of view. From the observed heat flow $\varphi(T)$, it is concluded that both *Pbam*-IM and *R*3*c*-IM transitions are endothermic. The Helmholtz free energy is given by

$$F(T) = U - TS(T), \tag{1}$$

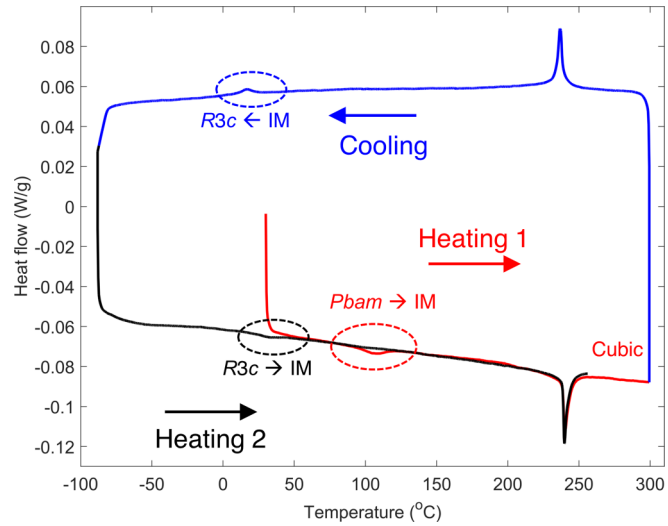


FIG. 7. Heat flow $\varphi(T)$ measured by DSC on $PbZr_{0.95}Ti_{0.05}O_3$ ceramic powder for heating (Heating 1, red curve), cooling (blue curve), and reheating (Heating 2, black curve) processes. Two endothermic peaks on Heating 1 correspond to the *Pbam* IM and IM-cubic transitions, respectively. Upon cooling, two exothermal peaks indicate the cubic-IM and the IM$-$*R*3*c* transition. Upon further cooling, the *Pbam* structure does not reappear. On Heating 2, the *R*3*c*-IM and IM-cubic transitions are observed.

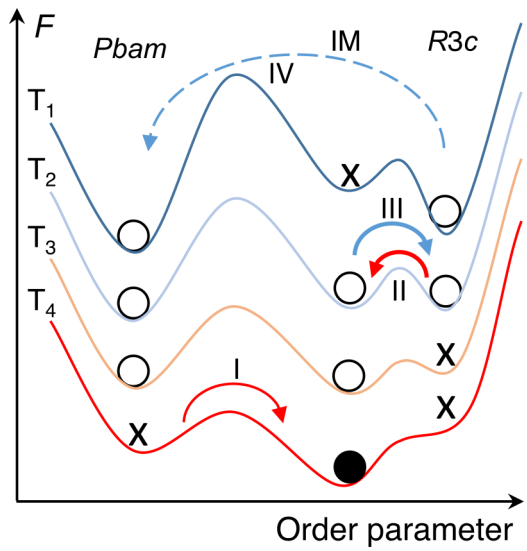


FIG. 8. A schematic plot of the energy landscapes at different temperatures. The arrows indicate the phase transition processes upon heating (red arrows) and cooling (blue arrows). The dashed blue line suggests that the IM → *Pbam* is a slow transition. The solid circle and the crosses indicate the stable phase and unstable phases, respectively. The open circles indicate the phases which can be stabilized depending on the thermal history.

where $U$ and $S(T)$ correspond to the internal energy and entropy. Upon a phase transition, the free energies $F(T)$ of both phases should be equivalent. The endothermic process indicates an increase in internal energy during the transition, and so the entropy is increased from the *Pbam*/*R*3*c* structures to the IM state. The larger entropy of the IM state is consistent with its complex local structure [17,29].

We demonstrate the transition of $x = 0.05$ by the schematic energy landscapes shown in Fig. 8. At a low temperature ($T_1$), both *Pbam* and *R*3*c* structures can be stabilized, depending on the thermal history. Upon heating, the free energies $F(T)$ of all three phases decrease, mainly caused by the entropic contribution $-TS$. The larger entropy of the IM state causes a larger slope $|\partial F/\partial T|$ than those of *Pbam* and *R*3*c* structures. Above $T_{\mathrm{IM}}$, the IM structure has a lower $F_{\mathrm{IM}}$ than that of the other phases and becomes more favorable, which should be the driving force for the *Pbam*-IM (red arrow I) and *R*3*c*-IM (red arrow II) transitions. Moreover, with increasing $x$ in AFE compositions, the internal energy of the IM structure decreases (Table II) and so stabilizing the IM state requires less entropic contribution, which explains the decreasing $T_{\mathrm{O}\rightarrow\mathrm{IM}}$ with the growing Ti concentration.

As for the unusual transition at $x = 0.05$ upon cooling, the energy barrier between high- and low-temperature phases determines the phase transition pace and temperature. As shown in optical and x-ray scattering experiments, the crystal structure changes discontinuously between the *Pbam* and IM structures, indicating a large energy barrier on the transition path. In contrast, the transitions between *R*3*c* and IM structures are continuous and smooth, indicating a much-smaller energy barrier. During first-principle optimization relaxed from the IM structure with $a^0\,a^0\,c^+$ tilts, after ~50 steps, we arrived at an energy plateau of the *Pc* space group, which was observed as a major phase in the IM structure [17] (Fig. S5 in the Supplemental Material [22]). Then the $a^-\,a^-\,a^-$ tilts start to develop slowly and smoothly, and we finally obtained the *R*3*c* structure. This process of optimization is similar to the IM−*R*3*c* transition process upon cooling, during which there may not be an energy barrier to overcome. At around $T_2$ on cooling, although the free energy of the *Pbam* phase is much lower than that of the IM phase, the thermal fluctuation around this relatively low temperature cannot help overcome the large barrier to jump from the IM state to the *Pbam* phase. Instead, there is a higher possibility that the IM state jumps into the *R*3*c* phase which has similar free energy to the *Pbam* structure, passing through a shallow saddle (or no barrier at all), as marked by the blue arrow III. The stabilization of the slightly more stable *Pbam* structure requires a long time, as marked by the blue arrow IV.

In compositions with smaller $x$, the energy barrier between *Pbam* and IM structures should be similar to that of $x = 0.05$, while the thermal hysteresis of the *Pbam* ⇔ IM transitions decreases, and this should be related to the increased $T_{\mathrm{IM}}$ of the *Pbam* ⇔ IM transition. At a higher $T_{\mathrm{IM}}$, with larger entropy, the contribution from the term $-TS$ to the free energy becomes more significant than at lower temperatures, so that the energy landscape changes more violently upon changing temperature. Moreover, at higher temperatures, the thermal fluctuation is larger than that at a lower temperature. Thus the jump from one phase to another happens more easily and faster during this first-order transition, which enables the AFE structures to be stabilized within a shorter time.

## V. CONCLUSION

We have clarified the complex phase transitions near the *Pbam*-*R*3*c* boundary of PZT using multiple experimental methods and DFT calculation. On both the AFE and FE sides far from the phase boundary, the crystal structures are stable at RT, with simple transition processes at reproducible transition temperatures. As $x$ increases from 0.04 to near the *Pbam*-*R*3*c* phase boundary, the AFE component becomes continuously less stable, reflected in the way that the AFE domains shrink, becoming abnormal microsized domains and eventually appearing as local components only. At $x = 0.04$, we observe the coexistence of large and microsized AFE domains before heating. On cooling, the microdomains appear after the IM → *Pbam* transition finishes, and this domain activity is also observed from DS (Fig. S6 in the Supplemental Material). At certain temperatures, the quarter-reflection intensity from one type of domain is strengthened while another is weakened at the same time. This temperature may coincide with that of the appearance of microsized AFE domains, similar to what is shown in Fig. S3 in the Supplemental Material [22]. At $x = 0.05$, all the AFE domains are small, coexisting with a small amount of *R*3*c* structure at RT before heating, while they only appear from prolonged phase transitions after cooling. The FE structure becomes more favored at $x \geqslant 0.06$ in which a small proportion of AFE structure (if there is any) exists as local-structural components invisible under an optical microscope. The observed phase transitions are caused by the combination of internal energies and entropic contributions of different phases in competition. The decreased

energy difference between the room-temperature AFE phase and the IM state leads to a lower transition temperature in the $x = 0.05$ sample. At the same time, the smaller thermal fluctuation and milder entropy change at lower temperatures make it take a longer time for the system to overcome the large energy barrier between the *Pbam* and IM/*R*3*c* structures upon cooling. The unusual transition at $x = 0.05$ provides us with the opportunity to study the slow nucleation and growth of AFE domains, which usually happens too quickly to be observed.

Based on this unusual transition path $Pbam \xrightarrow{\text{heating}} \text{IM} \xrightarrow{\text{cooling}} R3c \xrightarrow{\text{resting}} Pbam$ at the *Pbam*-*R*3*c* phase boundary, we see a subtle balance between *Pbam* and *R*3*c* structures when cooled down from the IM state, which may be perturbed by a slight change in the concentration or other external stimuli [10,30,31]. The direct observation of the transition between such different crystal structures, FE *R*3*c* and AFE *Pbam*, gives us a clear direction for the potential of controlling the physical property change during the phase transition, which opens up a broad range of future applications.

## ACKNOWLEDGMENTS

N.Z., Z.A., and S.X. are supported by the NSFC (Grants No. 12074304 and No. 12161141012) and the "111 Project" of China (Grant No. B14040). M.P., P.O., and P.M. are supported by the Strategy AV21 framework of the Czech Academy of Sciences, program "Efficient Energy Conversion and Storage and Operational Programme Research, Development and Education" financed by European Structural and Investment Funds and the Czech Ministry of Education, Youth and Sports (Project No. SOLID21-CZ.02.1.01/0.0/0.0/16_019/0000760). For the synchrotron experiment at Elettra, support was received under the CALIPSOplus project under the Grant Agreement No. 730872 from the EU's HORIZON 2020 research and innovation framework program. Computational resources were supplied by the project "e-Infrastruktura CZ" (e-INFRA CZ LM2018140) supported by the Ministry of Education, Youth and Sports of the Czech Republic. Z.-G.Y. acknowledges the support from the U.S. Office of Naval Research (ONR, Grant No. N00014-16-1-3106) and the Natural Sciences and Engineering Research Council of Canada (NSERC, Grant No. RGPIN-2017-06915). We are also grateful to Elettra Sincrontrone Trieste for access to Beamline X-Ray Diffraction I (experimental session No. 20195557), the ISIS neutron spallation source for the HRPD instrument (experimental session No. 2010305), and Shanghai Synchrotron Radiation Facility for access to Beamline BL02U2. We thank P. Vaněk for the fruitful discussion of the DSC measurements.

[1] D. Damjanovic, Contributions to the piezoelectric effect in ferroelectric single crystals and ceramics, J. Am. Ceram. Soc. **88**, 2663 (2005).

[2] B. Noheda, D. E. Cox, G. Shirane, J. A. Gonzalo, L. E. Cross, and S.-E. Park, A monoclinic ferroelectric phase in the $Pb(Zr_{1-x}Ti_x)O_3$ solid solution, Appl. Phys. Lett. **74**, 2059 (1999).

[3] N. Zhang, H. Yokota, A. M. Glazer, Z. Ren, D. A. Keen, D. S. Keeble, P. A. Thomas, and Z.-G. Ye, The missing boundary in the phase diagram of $PbZr_{1-x}Ti_xO_3$, Nat. Commun. **5**, 5231 (2014).

[4] A. S. Mischenko, Q. Zhang, J. F. Scott, R. W. Whatmore, and N. D. Mathur, Giant electrocaloric effect in thin-film $PbZr_{0.95}Ti_{0.05}O_3$, Science **311**, 1270 (2006).

[5] D. L. Corker, A. M. Glazer, J. Dec, K. Roleder, and R. W. Whatmore, A re-investigation of the crystal structure of the perovskite $PbZrO_3$ by x-ray and neutron diffraction, Acta Crystallogr., Sect. B **53**, 135 (1997).

[6] S. B. Vakhrushev, D. Andronikova, I. Bronwald, E. Y. Koroleva, D. Chernyshov, A. V. Filimonov, S. A. Udovenko, A. I. Rudskoy, D. Ishikawa, A. Q. R. Baron, A. Bosak, I. N. Leontiev, and A. K. Tagantsev, Electric field control of antiferroelectric domain pattern, Phys. Rev. B **103**, 214108 (2021).

[7] A. M. Glazer, The classification of tilted octahedra in perovskites, Acta Crystallogr., Sect. B **28**, 3384 (1972).

[8] A. K. Tagantsev, K. Vaideeswaran, S. Vakhrushev, A. V. Filimonov, R. G. Burkovsky, A. Shaganov, D. A. Andronikova, A. I. Rudskoy, A. Q. R. Baron, H. Uchiyama, D. Y. Chernyshov, A. Bosak, Z. Ujma, K. Roleder, A. Majchrowski, J.-H. Ko, and N. Setter, The origin of antiferroelectricity in $PbZrO_3$, Nat. Commun. **4**, 2229 (2013).

[9] J. Hlinka, T. Ostapchuk, E. Buixaderas, C. Kadlec, P. Kužel, I. Gregora, J. Kroupa, M. Savinov, A. Klic, J. Drahokoupil, I. Etxebarria, and J. Dec, Multiple Soft-Mode Vibrations of Lead Zirconate, Phys. Rev. Lett. **112**, 197601 (2014).

[10] J. Íñiguez, M. Stengel, S. Prosandeev, and L. Bellaiche, First-principles study of the multimode antiferroelectric transition in $PbZrO_3$, Phys. Rev. B **90**, 220103(R) (2014).

[11] H. Yokota, N. Zhang, A. E. Taylor, P. A. Thomas, and A. M. Glazer, Crystal structure of the rhombohedral phase of $PbZr_{1-x}Ti_xO_3$ ceramics at room temperature, Phys. Rev. B **80**, 104109 (2009).

[12] F. Cordero, F. Craciun, F. Trequattrini, C. Galassi, P. A. Thomas, D. S. Keeble, and A. M. Glazer, Splitting of the transition to the antiferroelectric state in $PbZr_{0.95}Ti_{0.05}O_3$ into polar and antiferrodistortive components, Phys. Rev. B **88**, 094107 (2013).

[13] F. Cordero, F. Trequattrini, F. Craciun, and C. Galassi, Effects of aging and annealing on the polar and antiferrodistortive components of the antiferroelectric transition in $PbZr_{1-x}Ti_xO_3$, Phys. Rev. B **89**, 214102 (2014).

[14] G. Shirane and S. Hoshino, Crystal structure of the ferroelectric phase in $PbZrO_3$ containing Ba or Ti, Phys. Rev. **86**, 248 (1952).

[15] J.-H. Ko, M. Górny, A. Majchrowski, K. Roleder, and A. Bussmann-Holder, Mode softening, precursor phenomena, and intermediate phases in $PbZrO_3$, Phys. Rev. B **87**, 184110 (2013).

[16] B. A. Scott and G. Burns, Crystal growth and observation of the ferroelectric phase of $PbZrO_3$, J. Am. Ceram. Soc. **55**, 331 (1972).

[17] Z. An, H. Yokota, N. Zhang, M. Paściak, J. Fábry, M. Kopecký, J. Kub, G. Zhang, A. M. Glazer, T. R. Welberry, W. Ren, and Z.-G. Ye, Multiple structural components and their

competition in the intermediate state of antiferroelectric Pb(Zr, Ti)$O_3$, Phys. Rev. B **103**, 054113 (2021).

[18] J. H. Hubbell and S. M. Seltzer, Tables of x-Ray Mass Attenuation Coefficients and Mass Energy-Absorption Coefficients 1 keV to 20 MeV for Elements $Z = 1$ to 92 and 48 Additional Substances of Dosimetric Interest, No. NISTIR-5632 NIST (1995), http://physics.nist.gov/PhysRefData/XrayMassCoef/cover.html.

[19] V. Dyadkin, P. Pattison, V. Dmitriev, and D. Chernyshov, A new multipurpose diffractometer PILATUS@SNBL, J. Synchrotron Radiat. **23**, 825 (2016).

[20] A. A. Coelho, A bound constrained conjugate gradient solution method as applied to crystallographic refinement problems, J. Appl. Crystallogr. **38**, 455 (2005).

[21] H. Rietveld, A profile refinement method for nuclear and magnetic structures, J. Appl. Crystallogr. **2**, 65 (1969).

[22] See Supplemental Material at http://link.aps.org/supplemental/10.1103/PhysRevB.106.224103 for more details on crystal structure, domain structure, and calculated energy.

[23] F. Cordero, F. Trequattrini, F. Craciun, and C. Galassi, Merging of the polar and tilt instability lines near the respective morphotropic phase boundaries of $PbZr_{1-x}Ti_xO_3$, Phys. Rev. B **87**, 094108 (2013).

[24] Z. An, S. Xie, N. Zhang, J. Zhuang, A. M. Glazer, W. Ren, and Z.-G. Ye, Ferroelastic domain hierarchy in the intermediate state of $PbZr_{0.98}Ti_{0.02}O_3$ single crystal, APL Mater. **9**, 030702 (2021).

[25] R. W. Whatmore, R. Clarke, and A. M. Glazer, Tricritical behaviour in $PbZr_xTi_{1-x}O_3$ solid solutions, J. Phys. C: Solid State Phys. **11**, 3089 (1978).

[26] D. A. Andronikova, I. A. Bronwald, N. G. Leontyev, I. N. Leontyev, D. Y. Chernyshov, A. V. Filimonov, and S. B. Vakhrushev, Structural peculiarities of the intermediate phase in Zr-rich lead zirconate titanate, Phys. Solid State **61**, 1772 (2019).

[27] J. M. Soler, E. Artacho, J. D. Gale, A. García, J. Junquera, P. Ordejón, and D. Sánchez-Portal, The SIESTA method for *ab initio* order-*N* materials simulation, J. Phys.: Condens. Matter **14**, 2745 (2002).

[28] I. Grinberg, V. Cooper, and A. Rappe, Oxide chemistry and local structure of $PbZr_xTi_{1-x}O_3$ studied by density-functional theory supercell calculations, Phys. Rev. B **69**, 144118 (2004).

[29] Z. Fu, X. Chen, Z. Li, T. Hu, L. Zhang, P. Lu, S. Zhang, G. Wang, X. Dong, and F. Xu, Unveiling the ferrielectric nature of $PbZrO_3$-based antiferroelectric materials, Nat. Commun. **11**, 3809 (2020).

[30] S. E. Reyes-Lillo and K. M. Rabe, Antiferroelectricity and ferroelectricity in epitaxially strained $PbZrO_3$ from first principles, Phys. Rev. B **88**, 180102(R) (2013).

[31] B. Xu, O. Hellman, and L. Bellaiche, Order-disorder transition in the prototypical antiferroelectric $PbZrO_3$, Phys. Rev. B **100**, 020102(R) (2019).